

PAPER • OPEN ACCESS

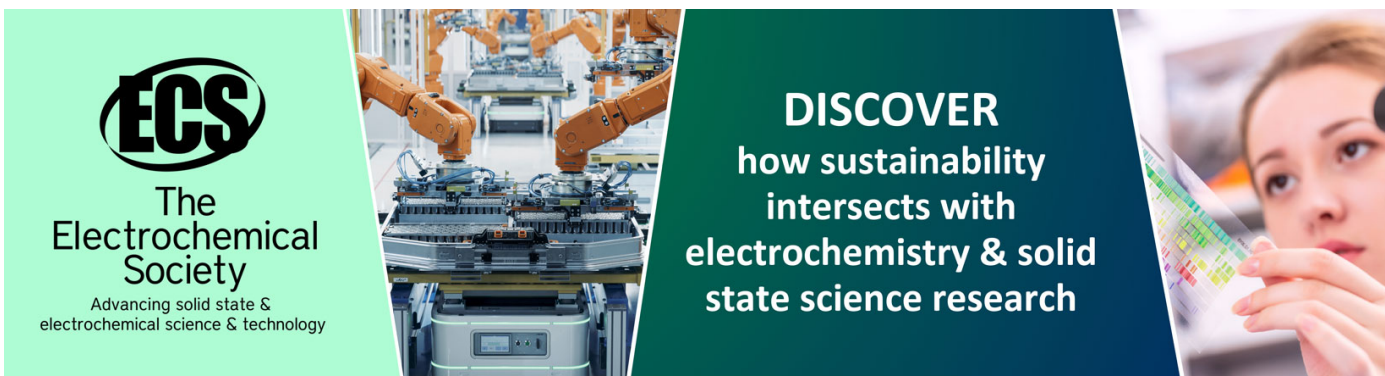
The study of lead vapor ionization in discharge with a hot cathode and efficiency of its deposition on the substrates applied for plasma separation method

To cite this article: N N Antonov *et al* 2016 *J. Phys.: Conf. Ser.* **774** 012196

View the [article online](#) for updates and enhancements.

You may also like

- [Power law fitting of the ion saturation current and the three-temperature Maxwellian EEDF in a multi-dipole confined hot cathode discharge: an experimental revisitiation](#)
Chi-Shung Yip, Chenyao Jin, Wei Zhang et al.
- [Passive blood plasma separation at the microscale: a review of design principles and microdevices](#)
Siddhartha Tripathi, Y V Bala Varun Kumar, Amit Prabhakar et al.
- [Diffuse arc discharge with a hot cathode in a magnetic field as a plasma source of lead and silver mixture for the problem of spent nuclear fuel reprocessing](#)
N N Antonov, R A Usmanov, A V Gavrikov et al.



ECS
The
Electrochemical
Society
Advancing solid state &
electrochemical science & technology

DISCOVER
how sustainability
intersects with
electrochemistry & solid
state science research

The study of lead vapor ionization in discharge with a hot cathode and efficiency of its deposition on the substrates applied for plasma separation method

N N Antonov, A A Samokhin, S N Zhabin, A V Gavrikov and
V P Smirnov

Joint Institute for High Temperatures of the Russian Academy of Sciences, Izhorskaya 13
Bldg 2, Moscow 125412, Russia

E-mail: antonovnickola@gmail.com

Abstract. Spent nuclear fuel plasma separation method approbation implies the use of model substances. Thus it is necessary to solve the problem of material conversion into a cold plasma flow, as well as the problem of deposition on collectors. For this purpose, we carried out a kinetic and hydrodynamic simulation of the discharge with hot cathode in the lead vapor (lead vapor was injected into the interelectrode gap). Dependencies of the ionization efficiency, electrostatic potential distribution, density distribution of ions and electrons in the discharge gap on the discharge current density and the model substance vapor concentration were obtained. The simulation results show that at discharge current density of about 3.5 A/cm^2 and the lead vapor concentration of $2 \times 10^{12} \text{ cm}^{-3}$, the ionization efficiency is close to 60%. Experimental research of the discharge with a hot cathode in the lead vapor was carried out. We also carried out the research of the Pb condensation coefficients on various substrates. For experimental data analysis the numerical model based on Monte Carlo method was used. The research results show that deposition coefficients at medium temperatures of substrates near 70°C do not drop lower than 75%.

1. Introduction

Increasing of the resource efficiency usage in the production cycles of electricity is one of the primary tasks for nuclear power industry. Plasma separation is one of the possible ways of solving the spent nuclear fuel (SNF) reprocessing problem. This method is developed nowadays [1, 2]. The essence of this approach is that the spent nuclear fuel from the condensed state is transferred to the low-temperature plasma flow (with ionization degree close to 100%) and then the flow is injected into the separation chamber, where in a special configuration of the electric and magnetic fields this flow is separated in space by mass into a groups of ions under-compensated volume charge [3]. Plasma sources of model substances, with high ionizing efficiency are needed to simulate experimentally the plasma separation method [4, 5]. It is also necessary to determine the effectiveness of the ionized elements deposition (condensation) on substrates. Lead was chosen to simulate dynamic properties of the heavy SNF components (minor actinides). The aim of this paper was the numerical and experimental study of the lead ionization and condensation processes.



2. Ionizing efficiency

2.1. Numerical model

This section presents the results of numerical modeling of the discharge in the lead vapor of concentration of $n_a = 10^{12}$ – 10^{13} cm $^{-3}$ in the gap between two flat electrodes received within the previously developed kinetic model taking into account the ionization cross section on energy dependence and the ion energy loss on a resonant recharging [6]. One of the electrodes was a hot cathode. The potential difference did not exceed value of 40 V (cathode potential $U_k = \varphi(0)$ and anode potential $U_a = \varphi(d)$, where d is the distance between electrodes and $\varphi(x)$ is electrostatic potential. The lead vapor was injected into the interelectrode space with an energy $\varepsilon_a = 0.1$ eV (figure 1).

The discharge in the lead vapor at low current densities ($J_e < 100$ mA/cm 2) was studied numerically and analytically in paper [6]. Cases in which ($n_e < n_i$; $E(d) = E_a = 0$) and ($n_e > n_i$; $E(0) = E_k = 0$) (where n_e is the electron concentration, n_i is the ion concentration and $E(x)$ is the electric field between the electrodes) were considered there. However, it is a also possible situation when the electric field strength between the cathode and the anode becomes 0 and a local maximum potential point arises (figure 2). This case of the electrostatic potential distribution in the interelectrode space with electron current densities J_e from 0.2 A/cm 2 to 4 A/cm 2 was considered in this paper.

Consider the neighborhood of the local maximum potential point ($x_0, \varphi = \varphi_{\max}$, see figure 2). Secondary electrons trapped in the potential well depth $\varphi_{\max} - \varphi_A$ was not considered (i.e. the region to the right of the maximum potential point was not considered, see figure 2). The directional movement of lead vapor can be neglected. If we use parabolic approximation of the potential in the neighborhood of x_0 point:

$$\varphi(x) = \varphi_{\max} - \frac{1}{2}c(x - x_0)^2,$$

where $c = \varphi''(x_0)$ then the equation for the ion concentration becomes [6]:

$$n_i(x) = \sqrt{\frac{m_i}{ck_B}} J_e \alpha_i(\Phi) F(k|x - x_0|),$$

$$F(\lambda) = e^\lambda \int_0^1 (1 + \lambda\xi) e^{-\lambda\xi} \frac{d\xi}{\sqrt{1 - \xi^2}} \cong \frac{1}{2} \pi e^\lambda (1 - \frac{1}{2} \lambda^2),$$

where $\alpha_i(\Phi) = n_a \sigma_i(\Phi)$, n_i is singly charged ion density, k is resonant charge exchange coefficient ($n_a \sigma_{\text{exch}}$), Φ is energy of the electrons at the x_0 point, σ_{exch} is resonant charge exchange cross-section, k_B is Boltzmann constant and σ_i is Pb ionization cross-section. $\Phi > \varphi_{\max}$ because the electrons were injected into the interelectrode space with initial energy $\varepsilon_e = 8.4$ eV.

The constant c definition equation and ion density expression in the x_0 point depending on n_a , J_e and Φ follows from Poisson's equation for the potential [6]:

$$\frac{c}{\beta J_e} = \frac{\pi}{\sqrt{2}} \frac{\alpha_i(\Phi)}{\sqrt{c}} - \sqrt{\frac{m_e}{m_i}} \frac{1}{\sqrt{\Phi}},$$

$$\beta = 36 \times 10^{11} \pi \sqrt{\frac{m_i}{2k_B}} = 0.81 \times 10^7 \sqrt{A}, \quad (1)$$

$$n_i(x_0) = \frac{\pi}{2} \sqrt{\frac{m_i}{ck_B}} \frac{J_e \alpha_i(\Phi)}{\sqrt{c}} = 10^{13} \sqrt{A} \frac{J_e \alpha_i(\Phi)}{\sqrt{c}}.$$

The ion density in the maximum potential point is different from 0 under the previously made assumptions.

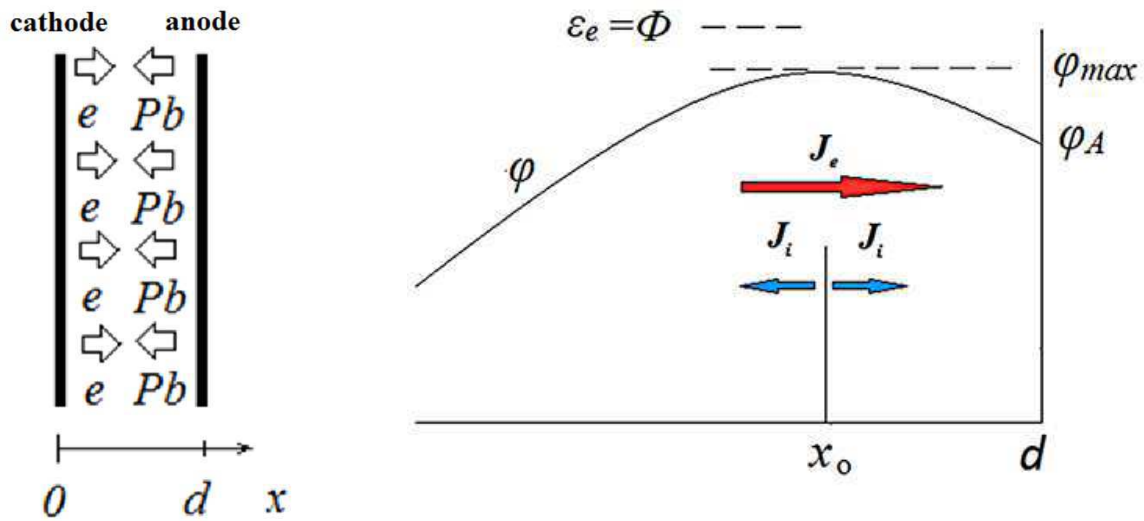


Figure 1. The modeling scheme.

Figure 2. Space near the anode: electric field and current are equal to 0 in x_0 point, $E(x_0) = 0$, $J_i = 0$.

Equations (1) allow to pass from boundary condition problem which was considered in [6], to the Cauchy problem with the same equations for the ion concentration, ion current, and potential. The initial conditions at the point of maximum potential are $j_i(x_0) = 0$ (ion current), $E(x_0) = 0$ (electric field) and $\varphi(x_0) = \varphi_{max} = 0$ (potential). J_e , n_i and Φ were considered as the set parameters during the calculation. The equation system has the form:

$$-\frac{dj_i}{dx} = n_a \sigma_{+1}(\varphi) J_e,$$

$$f_i(\varphi, \varepsilon) = -\frac{1}{E(x')} \frac{d}{dx'} [e^{n_a \sigma_{\text{exch}}(x-x')} j_i(x')],$$

$$n_i(x) = -4.5 \times 10^{12} \sqrt{A} \int_x^d \frac{d}{dx'} \left(e^{n_a \sigma_{\text{exch}}(x-x')} j_i(x') \right) \frac{dx'}{\sqrt{(\varphi(x') - \varphi(x)) + \varepsilon_a}},$$

$$\frac{d^2 \varphi}{dx^2} = \beta J_e \left(\sqrt{\frac{m_e}{m_i}} \frac{1}{\sqrt{\varphi}} - \int_x^d e^{n_a \sigma_{\text{exch}}(x-x')} \frac{\sigma_{+1}(\varphi(x')) + n_a \sigma_{\text{exch}} V_i(x')}{\sqrt{(\varphi(x') - \varphi(x)) + \varepsilon_a}} n_a dx' \right),$$

$$\beta = 36 \times 10^{11} \pi \sqrt{\frac{m_i}{2k_B}} = 0.81 \times 10^7 \sqrt{A} \left(\frac{VeV^{1/2}}{A} \right),$$

where σ_{+Z} is Z-degree ionization cross section, $f_i(\varphi, \varepsilon)$ is spectral density of the ions (A/(cm²eV)), ε is the ion energy at coordinate x with potential $\varphi(x)$, ε_a is the average kinetic energy of the neutral particles of the vapor, A is atomic mass and $\varphi(x') = \varphi(x) + (\varepsilon - \varepsilon_a)$, $V_i(U) = \int_0^U (\sigma_i(\varphi)/E(U, \varphi)) d\varphi$, $\sigma_i = \sigma_{+1}(\varphi) + 2\sigma_{+2}(\varphi) + \dots + i\sigma_{+i}(\varphi)$ is the total lead ionization cross section and $E(U, \varphi) = (4/3)U^{3/4}\varphi^{1/4}/d$ [6].

2.2. Calculation results

Figure 3 shows the results of numerical modeling of the potential, energy of the ions and the electric field strength in the interval $(0; x_0)$. Figure 4 shows the electron density, ion density and single and double ionization efficiency η (η is an ion flow of appropriate ion multiplicity to neutral flow of atoms ratio) at current density of $J_e = 0.2$ A/cm² and the vapor concentration of $n_a = 10^{13}$ cm⁻³.

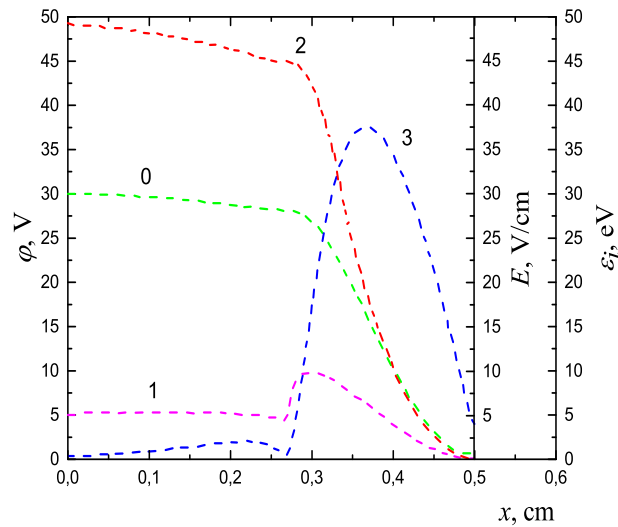


Figure 3. Potential $-\varphi$ (curve 0), ion energy ε_i Pb^+ (curve 1) and ion energy Pb^{2+} (curve 2), electric field intensity E (curve 3). Electron energy at the x_0 point $\Phi = 38$ eV, electron energy on the cathode $\varepsilon_e = 8.4$ eV, potential difference between the cathode and the x_0 point 29.6 V, $n_a = 10^{13} \text{ cm}^{-3}$, $J_e = 0.2 \text{ A/cm}^2$.

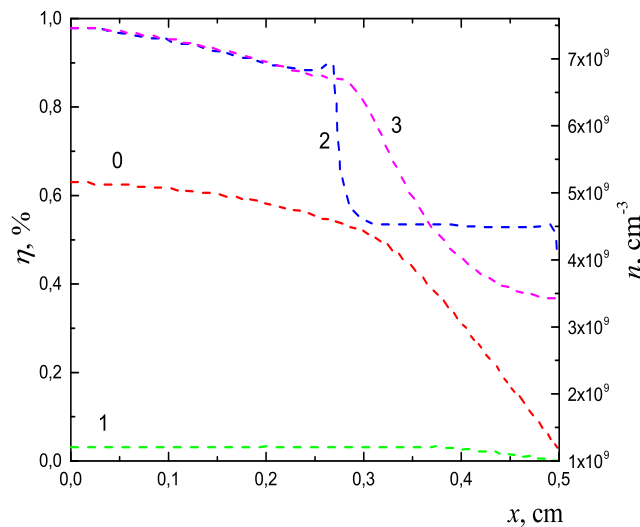


Figure 4. The single ionizing (curve 0) and double ionizing efficiency (curve 1), electron density n_e (curve 3) and the sum of the densities of singly and doubly ionized atoms (curve 2). Electron energy at the x_0 point $\Phi = 38$ eV, electron energy on the cathode $\varepsilon_e = 8.4$ eV, potential difference between the cathode and the x_0 point 29.6 V, $n_a = 10^{13} \text{ cm}^{-3}$, $J_e = 0.2 \text{ A/cm}^2$.

Figure 4 shows that the ionizing efficiency at such parameters is close to 0.6%. It should be noted that the potential maximum is reached at the distance of 0.5 cm from the cathode. Current density increase and vapor concentration decrease lead to a significant increase of ionizing efficiency.

Similar calculation for the electron current density of $J_e = 1 \text{ A/cm}^2$ and vapor concentration of $n_a = 2 \times 10^{12} \text{ cm}^{-3}$ is given in figures 5 and 6. Figure 6 shows that the single ionizing efficiency exceeds 15%. It is worth noting that at the same time double ionizing efficiency is not more than 1%. The potential maximum is reached at the distance of 2 cm from the cathode. The simulation results for the discharge current densities up to 4 A/cm^2 and vapor concentrations

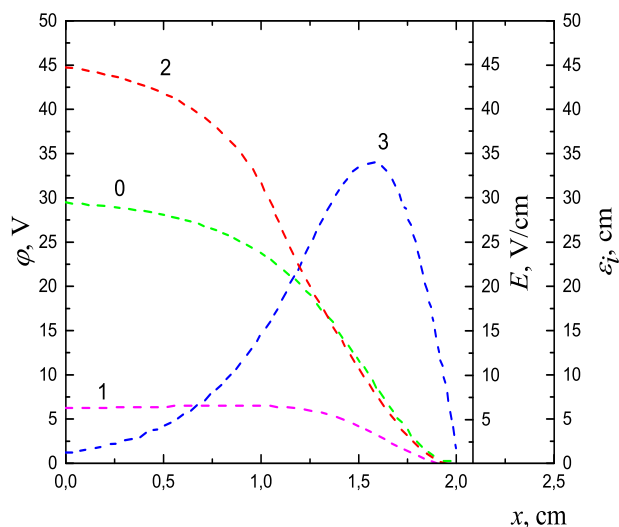


Figure 5. Potential $-\varphi$ (curve 0), ion energy $\varepsilon_i \text{ Pb}^+$ (curve 1) and ion energy Pb^{2+} (curve 2), electric field intensity E (curve 3). Electron energy at the x_0 point $\Phi = 38$ eV, electron energy on the cathode $\varepsilon_e = 8.4$ eV, potential difference between the cathode and the x_0 point 29.6 V, $n_a = 2 \times 10^{12} \text{ cm}^{-3}$, $J_e = 1 \text{ A/cm}^2$.

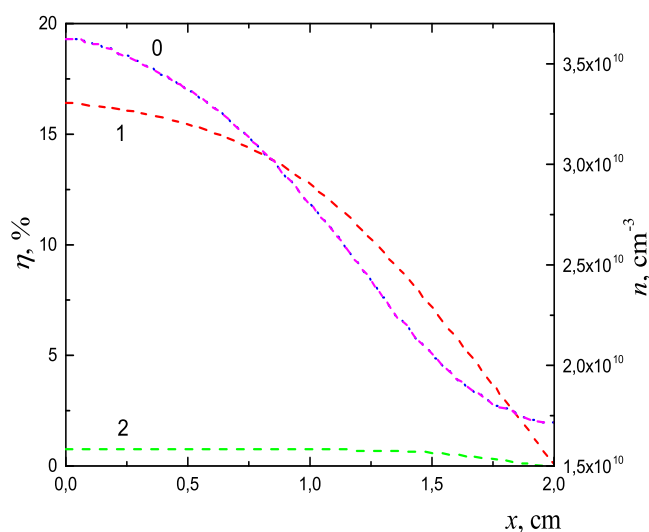


Figure 6. The single ionizing (curve 1) and double ionizing efficiency (curve 2), electron density n_e (curve 0) and the sum of the densities of singly and doubly ionized atoms (curve 0). Electron energy at the x_0 point $\Phi = 38$ eV, electron energy on the cathode $\varepsilon_e = 8.4$ eV, potential difference between the cathode and the x_0 point 29.6 V, $n_a = 10^{13} \text{ cm}^{-3}$, $J_e = 0.2 \text{ A/cm}^2$.

of $n_a = 2 \times 10^{12} \text{ cm}^{-3}$ and $n_a = 10^{13} \text{ cm}^{-3}$ are shown in figure 7 ($x_0 = 1 \text{ cm}$). Figure 7 shows that the single ionizing efficiency reaches 60% ($\Phi = 38$ eV, $n_a = 2 \times 10^{12} \text{ cm}^{-3}$, $J_e = 3.5 \text{ A/cm}^2$).

The simulation results show that the model substance plasma source with ionization effectiveness at the level of several tens of percent can be created. Source with such ionizing efficiency parameters allows to carry out pilot plasma separation experiments of model substances.

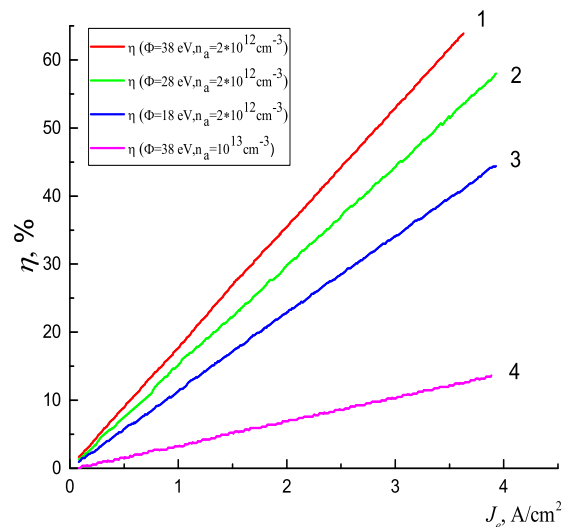


Figure 7. The single ionizing efficiency depending upon the current density J_e , cathode–anode potential difference and lead vapor concentration in the interelectrode gap. Initial electron energy on the cathode $\varepsilon_e = 8.4$ eV. The single ionizing efficiency: 1) $\Phi = 38$ eV and $n_a = 2 \times 10^{12}$ cm⁻³, 2) $\Phi = 28$ eV and $n_a = 2 \times 10^{12}$ cm⁻³, 3) $\Phi = 18$ eV and $n_a = 2 \times 10^{12}$ cm⁻³, 4) $\Phi = 38$ eV and $n_a = 10^{13}$ cm⁻³.

2.3. Experiment

For experimental studying of model substance ionization processes the experimental module was designed and series of experiments was carried out.

The experimental module consists of two main parts: the evaporator cell and the ionization unit. The experimental scheme is shown in figure 8. Evaporation of the model substance was carried out by a crucible heating (designation 1 in figure 8). The material flow injecting into the ionization area was formed by a hole of 1.1 mm in diameter (designation 7 in figure 8). The maximum temperature inside the evaporator cell was 1450 K. Ionization unit is a system consisted of three electrodes: electron emitter (designation 5 in figure 8), electron collector (designation 4 in figure 8) and ion collector (designation 3 in figure 8). It is worth noting that in the considered calculation model ionizing system consists of two plane electrodes but in the experiment an ion collector was added to them. This collector is necessary for measuring the number of ions produced in the discharge region. In our experiments the potential difference between the electron collector (designation 4 in figure 8) and the electron emitter (designation 5 in figure 8) did not exceed 350 V. The design of the hot cathode was developed so that distribution of electric field in a gap between the electron collector and the thermocathode was close to the field of the plane capacitor. These parameters were satisfied by the system of two parallel-connected tungsten filament 200 microns in diameter and the flat U-shaped stainless steel plate (see figure 8). The distance from the evaporator hole to the ionization region was 1.5 cm. The distance from the thermionic filaments to the diagnostic ion collector was 0.5 cm. The distance from thermocathode to the electron collector was 1 cm. Air was used as a buffer gas. Its residual pressure did not exceed 10^{-4} Torr.

In the initial stage of the experiment the potentials of electrodes (ion collector $U_i = -50$ V, thermionic filaments and U-shaped plate $U_c = 5$ V, evaporator $U_{cr} = 0$) were held constant. After that the measurements of the diode I – V curve were done (residual pressure was 10^{-4} Torr). The electrodes working area s was defined by comparison the I – V curve with the Child-Langmuir law [7–9] (in the flat electrodes case). The working electrode area was $s = 1.6$ cm². In the main part of the experiment, lead was heated in the evaporation cell ($U_e = 350$ V,

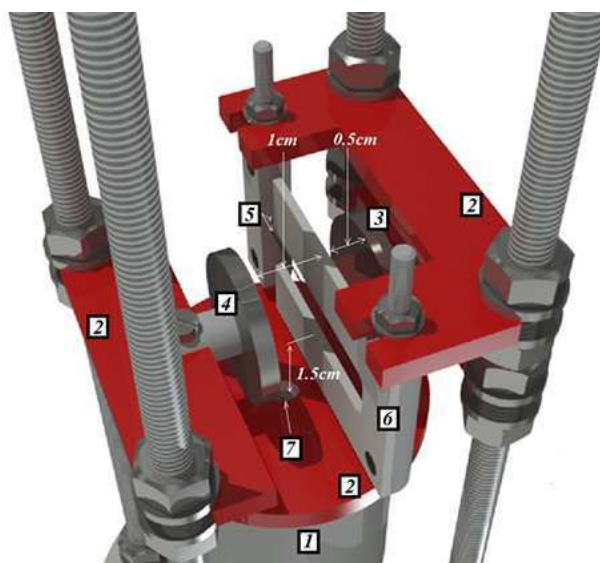


Figure 8. Experimental installation: 1—Evaporator ($U_{cr} = 0$), 2—ceramic insulators, 3—ions collector ($U_i = -50$ V), 4—electrons collector (initial $U_e = 350$ V), 5—thermionic filaments ($U_c = 5$ V), 6—U-shaped plate ($U_c = 5$ V) which is necessary for generating the electric field distribution close to the field of plane capacitor, 7—apertures for lead vapor injection.

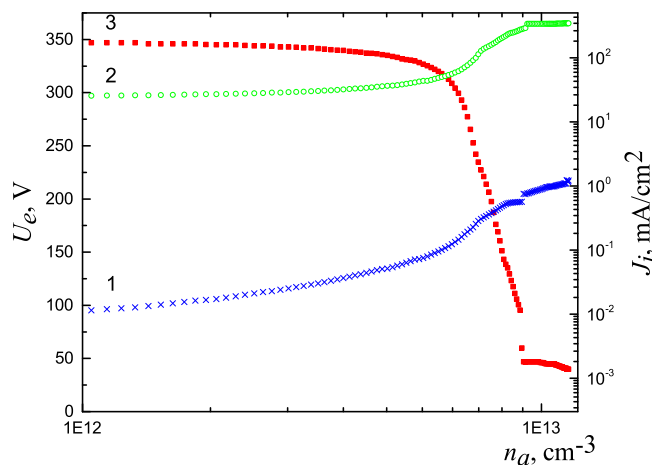


Figure 9. Dependence of the ion current J_i density (curve 1), electron current J_e density (curve 2) and potential difference in the discharge gap (curve 3) on concentration n_a of lead vapors in the ionization region.

$U_i = -50$ V, $U_c = 5$ V and $U_{cr} = 0$ were held constant). During the experiment the evaporation cell temperature and the J_e and J_i currents were measured. Evaluation of matter flow and concentration were based on the measurements of evaporation cell temperature and on the geometric parameters of the experiment.

Figure 9 shows the results of an experiment with parameters (discharge current density of 300 mA/cm² and a potential difference of about 40 V) close to the calculation parameters(see

figure 3 and 4). The results of the experiment shows that the ionizing efficiency η , which was obtained as an ion flow J_i to neutral flow of atoms ratio, is close to 1%. It can be seen that the experimental results are in agreement with the computational model ($\eta=0.6\%$). Thus, the model is verified by experimental data in the investigated range of parameters. This allows us to expect that predicted lead vapor ionizing efficiency (several tens of percent) can be obtained in the experiments. Plasma source developed on the basis of this discharge can be used for SNF plasma separation working off. It is worth noting that apart from the issue of creating a plasma source of model substance for plasma separation the separated materials collection question is significant. The matter flow reflection from the collector surface is possible. It can lead to incorrect interpretation of the obtained experimental data about matter flow. Therefore, the second part of this work is devoted to questions of lead deposition on the substrates.

3. Deposition efficiency

Deposition efficiency (i.e. particle deposition probability on a substrate at the first interaction) and adhesive properties of the films obtained on the collectors are important parameters from the plasma separation process point of view. It is necessary to avoid losses of separated substances. One needs to provide such conditions under which efficiency of deposition will be close to 100% or to create such geometry of collectors at which return of the separated substances to a volume of separation chamber will be minimum. Information about the adhesive properties allows us to choose an effective process of the coverings removal from the collectors.

The proposed concept of plasma separation [3] assumes that the energy of particles deposited on the collectors is small (less than 2 eV). This part of the work is based on the assumption that the interaction kinetics of the low-energy ions with substrates is close to condensation kinetics of the neutral vapor components with the thermal energy. Hence the coatings deposition in our experiments was carried out by the neutral atoms flow. It is worth noting that, according to published sources, re-evaporation occurs with equal probability in all half-space and does not depend on the incidence angle. Condensation efficiency is close to 100% when substrate consists of depositing material and its temperature is near liquid nitrogen temperature ($-195.75\text{ }^\circ\text{C}$) [10, 11].

The experiment scheme was developed for the model substance deposition efficiency on various substrates research. The essence of the experiment is that the collimated flow of lead neutral atoms entering the space between two flat disks after a certain number of impacts condensed on the upper or lower disk (the experiment scheme is shown in figure 10). The diameter of the disc should be much greater than the distance between them and much greater than the inlet diameter (designation 4 and 5 in figure 10). At the same time, free path length of the vapor must be much greater than inlet diameter. Execution of this ratios and conditions is significant because coatings deposition must be carried out in a molecular regime. It is possible to define deposition efficiency by means of the numerical model (described further) from the direct and reflect coatings profiles ratio (designation 3 and 2 in figure 10).

The experiment was conducted as follows. Lead was heated in the evaporator up to the temperature $950\text{ }^\circ\text{C}$. Air was used as a buffer gas. Its residual pressure does not exceed 2×10^{-5} Torr. Then the neutral collimated (inlet is 1.1 mm in diameter) atoms flow was directed into the space between the discs made of studied material (stainless steel and carbon). The distance between the disks during the experiment was 3.9 mm. Film deposition was carried out for about 30 minutes.

After the installation components cooling, substrates were removed from the vacuum chamber and were sent for analysis. In the initial stage of the experiments investigated substrate was cleaned by glow discharge. The thickness and profiles of the films were analyzed by scanning electron microscopy. The experimental results of the lead deposition on the stainless steel (Aisi 304) samples are shown in the figures 11, 12 and 13.

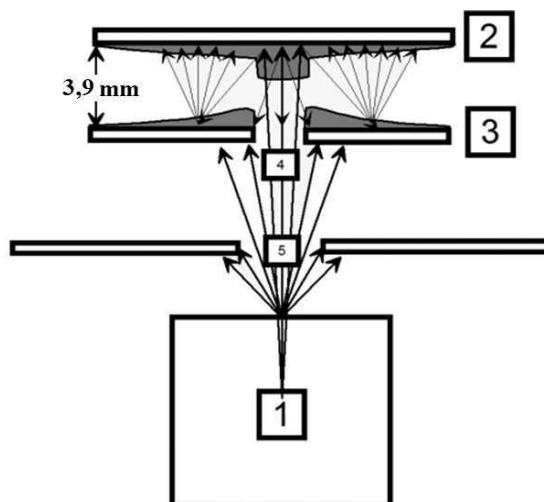


Figure 10. Experimental scheme: 1—evaporator, 2—sample (direct deposition surface), 3—sample (reflection deposition surface), 4 and 5—collimation apertures.

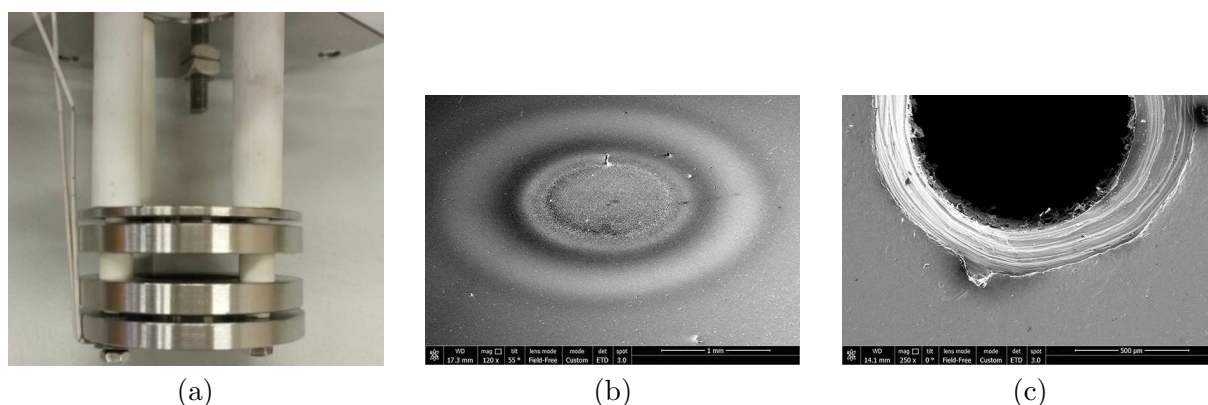


Figure 11. (a) Sample mounting unit; (b) Direct deposition surface (steel Aisi 304); (c) Reflection deposition surface (steel Aisi 304).

Figure 12a shows that agglomerations (with size up to 2 microns) were formed on the direct deposition surface. At the same time the minimal thickness of the direct deposition coverings was about $850 \mu\text{m}$ (see figure 12b). The covering thickness sizes presented in figure 12b need to be divided into $\sin(\theta = 55^\circ) \approx 0.82$, since the studied surface was placed at the 55 degrees angle to the diagnosing electron beam. During the sample scanning (from the center of direct deposition covering to the periphery) it was found that the agglomerations size decreases along the disc radius to 20 nm. At that the distance between the centers of agglomerations was larger than themselves (figure 12d).

Figure 13a shows the deposition covering consists of reflected atoms (disc 3 in figure 10). The size of the formed agglomerations was not more than 116 nanometers. Size of the agglomerations was decreased to 10 nanometers during the scanning along the radius (figure 13b). A numerical model based on the Monte Carlo method was created for the interpretation of the experimental data. The angular function of re-evaporation probability density, condensation probability, discs radius and distance between them are the key parameters of the numerical model. The angular function of re-evaporation probability density distribution and other parameters in a numerical

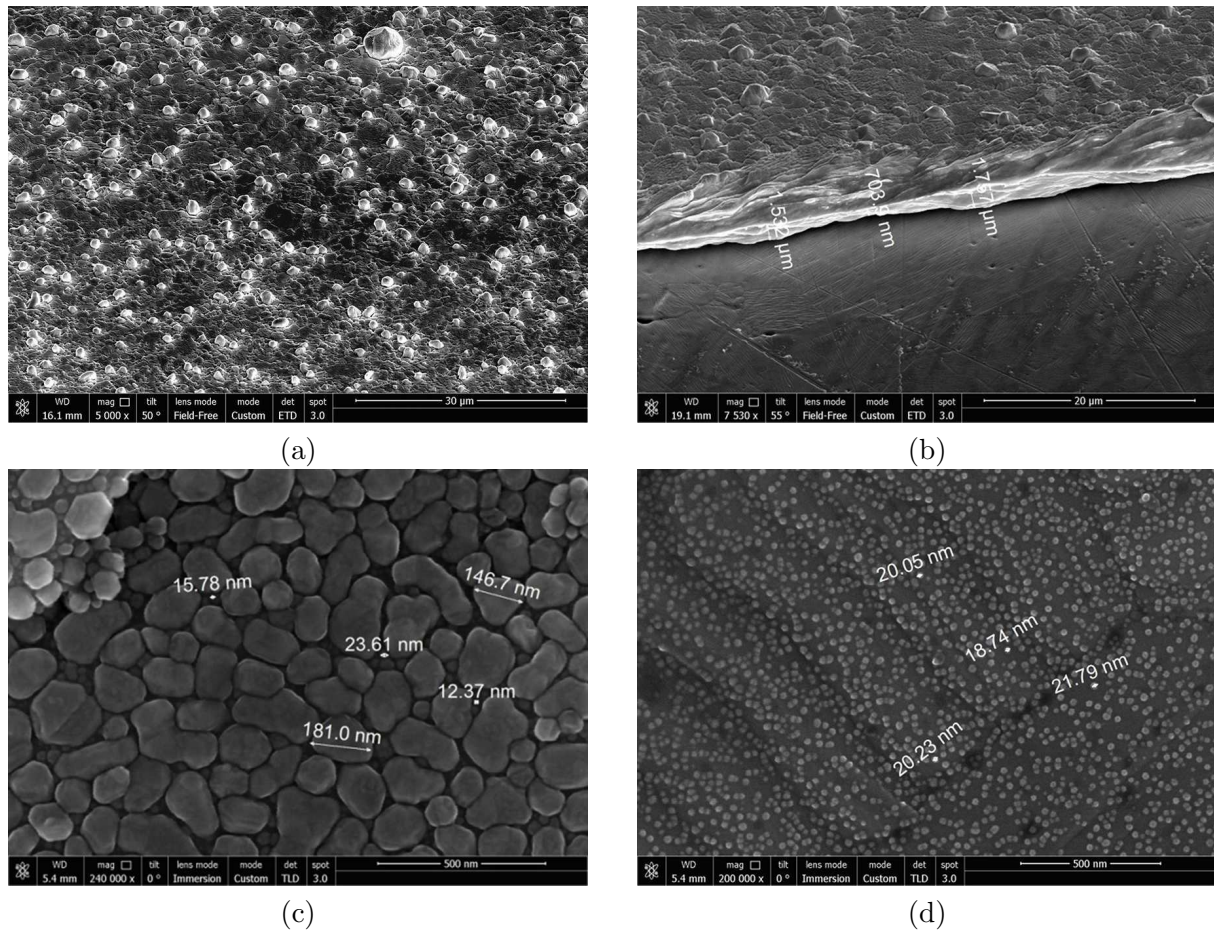


Figure 12. Disc 2 in figure 10: (a) direct deposition surface of the film. Agglomerations up to 2 microns are observed; (b) the film profile in the direct deposition area. Angle between the sample and diagnosing microscope beam was close to 55 degrees; (c) the film surface in the transition region. Transition region is an area between the reflected and direct deposition; (d) the film surface, consisting of a double-reflected particles.

model was chosen so that the results obtained in the model were the closest to the experimental data. The best fit of the experimental and numerical data observed with equally probable evaporation in a solid angle $2\pi/3$ along the normal to deposition surface.

Figure 14 shows the calculated profiles of direct (disk 2 in figure 10) and reflected (disk 3 the in figure 10) films deposition. Figure 15 shows the calculated dependence of the reflection covering thickness h_r (area near the inlet) to the thickness of the direct deposition covering h_d ratio on the probability of condensation in the first collision (deposition efficiency). Figure 15 shows that dependence is well approximated by linear function. It allows obtaining a formula for an assessment of deposition efficiency from the ratio of thickness of direct and reflected coverings:

$$\frac{h_r}{h_d} = 0.082(1 - P). \quad (2)$$

The use of a numerical model for the interpretation of the experimental data was hampered by heterogeneity of the films thickness. The conclusion of the deposition efficiency was made from the average size of the agglomerations and from the average values of films thicknesses. The average thickness of the direct deposition film in experiment with the stainless steel sample was

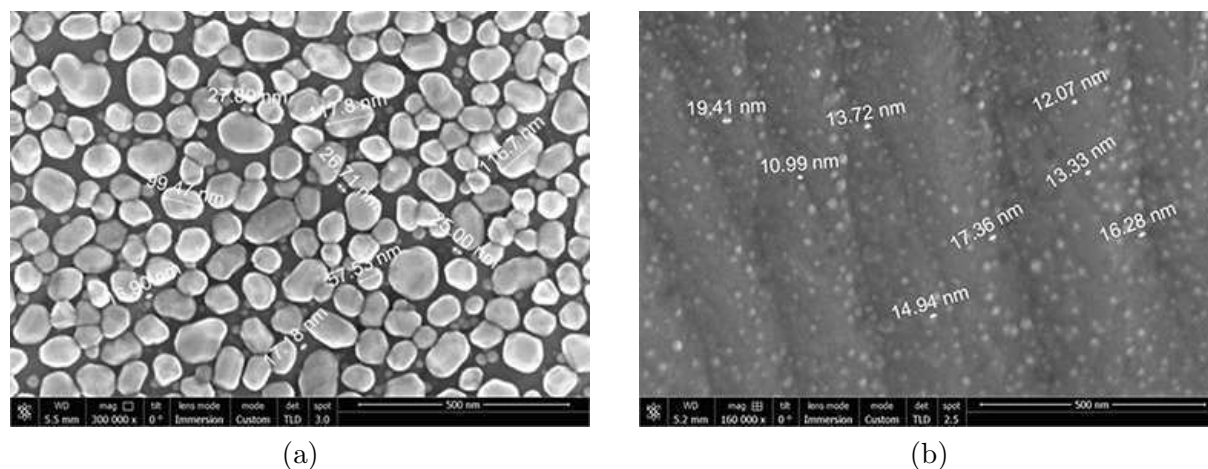


Figure 13. Disc 3 in figure 10: (a) reflection deposition surface of the film. Agglomerations up to 116 nanometers are observed; (b) reflection deposition surface of the film. Figure shows a region at a distance of 7 mm from the center of the sample.

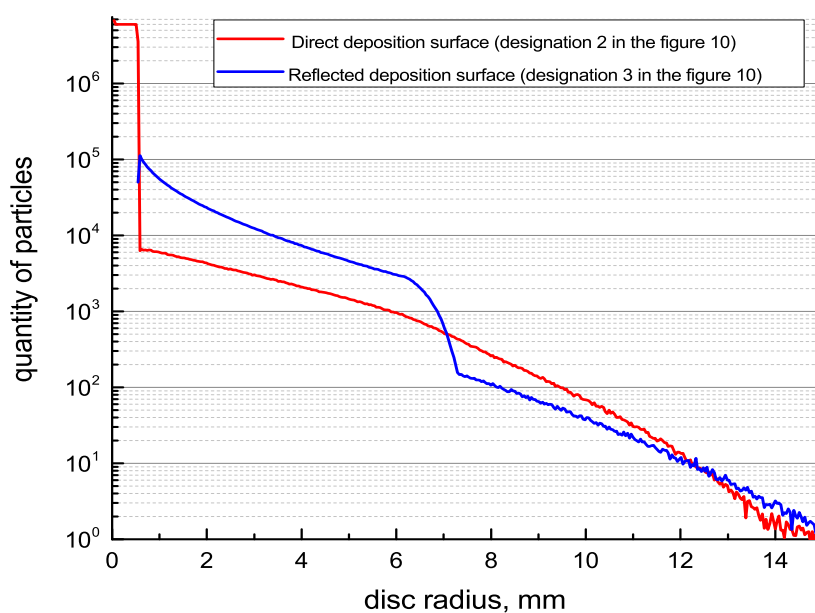


Figure 14. Films profiles obtained by numerical simulation.

1.75 μm and the thickness of the reflected deposition film near collimation inlet (distance from the disk center was about 750 microns) was 35 nm. Figure 15 and formula (2) show that the lead deposition efficiency on the stainless steel substrates is about 75%. The average substrate temperature during the experiment was about 70 $^{\circ}\text{C}$.

Similar experiments were carried out using the carbon substrates (figure 16a). Figure 16b shows that lead agglomerations on the surface of direct deposition have a size of about 1 micron. The size of agglomerations gradually decreases to a few nanometers during the scanning along the radius of disc (figure 16c and 16d). Figure 17a shows the deposition covering consists of reflected atoms (disc 3 in figure 10). The size of the formed agglomerations was not more than 40 nanometers. Size of the agglomerations was decreased to a few nanometers during the scanning along the radius (figure 17b).

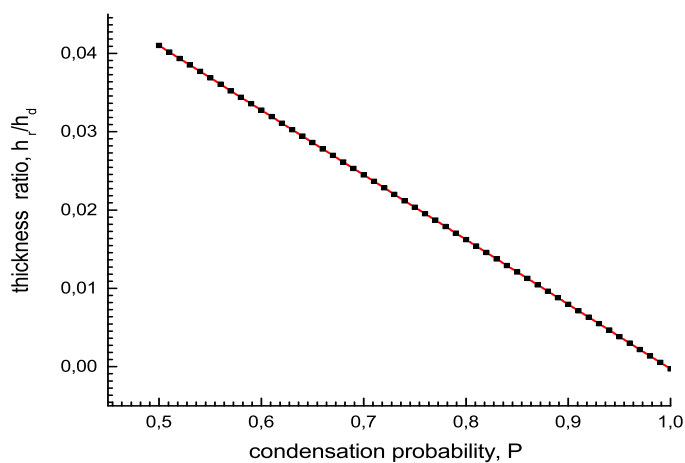


Figure 15. Dependence of the films thickness ratio h_r/h_d on the condensation probability (P).

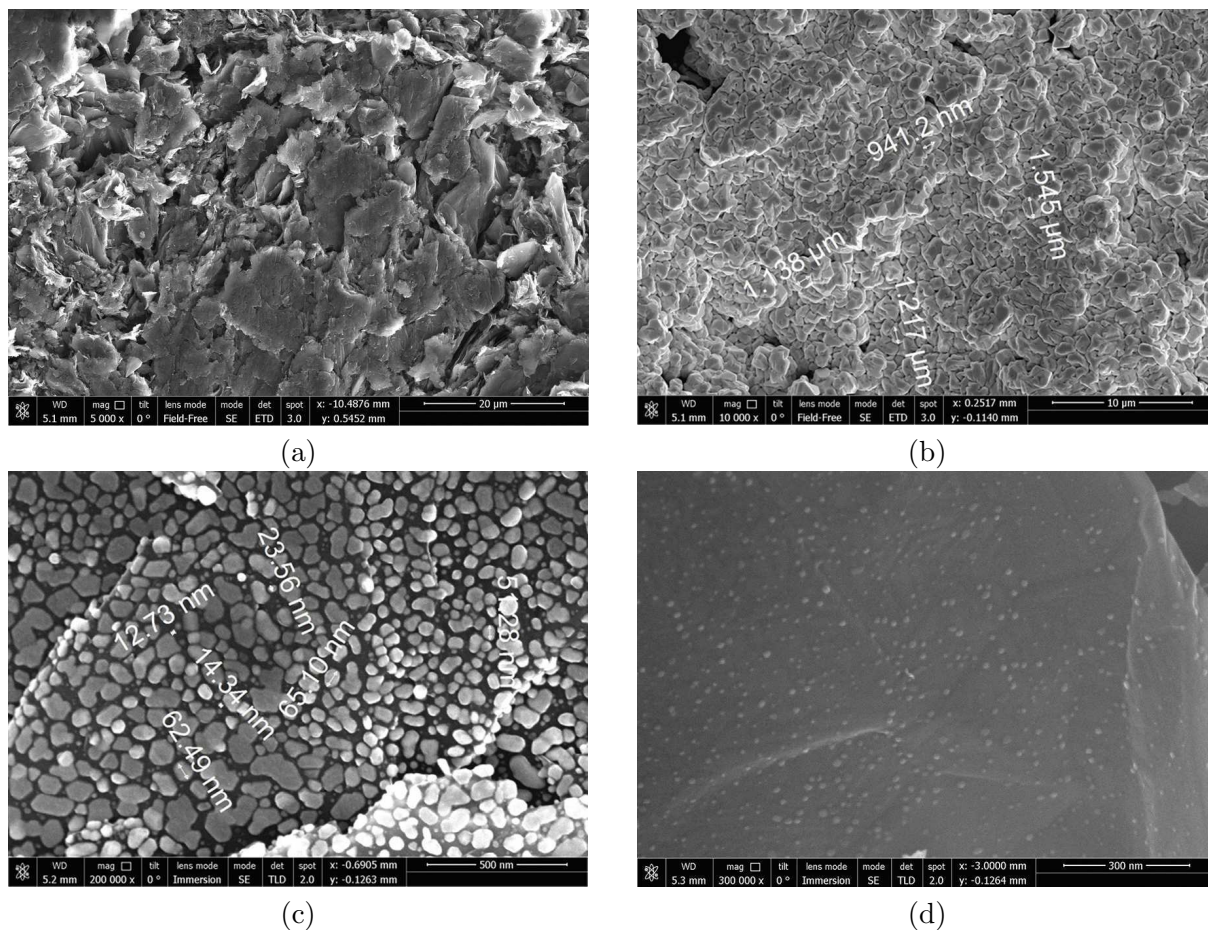


Figure 16. Disc 2 in figure 10: (a) carbon surface before the lead deposition; (b) direct deposition surface of the film. Agglomerations up to 1 microns are observed; (c) direct deposition surface of the film (1.5 mm from the center of the area of direct deposition); (d) direct deposition surface of the film (3.5 mm from the center of the area of direct deposition).

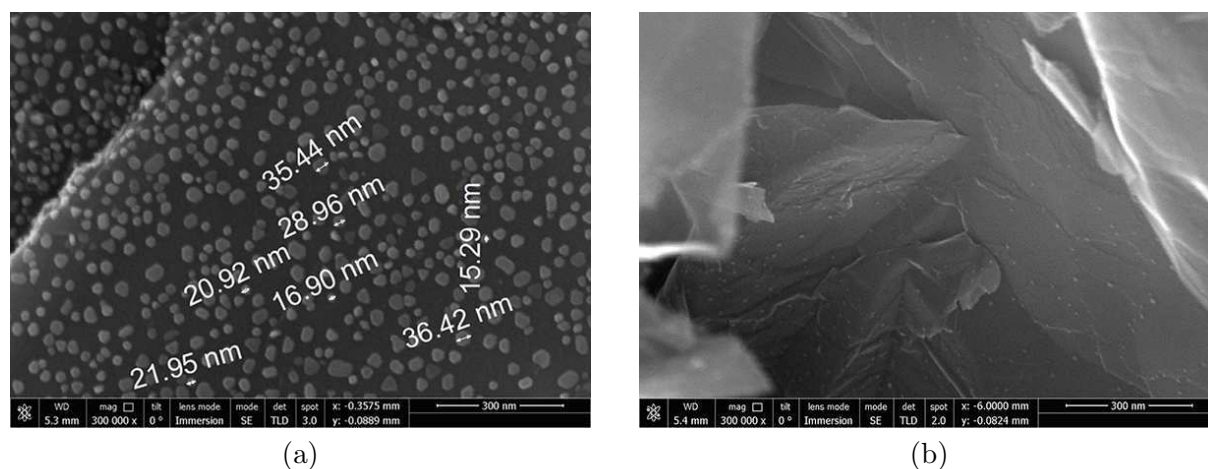


Figure 17. Disc 3 in figure 10: (a) reflection deposition surface of carbon substrates; (b) reflection deposition surface. Figure shows a region at a distance of 6 mm from the center of the sample.

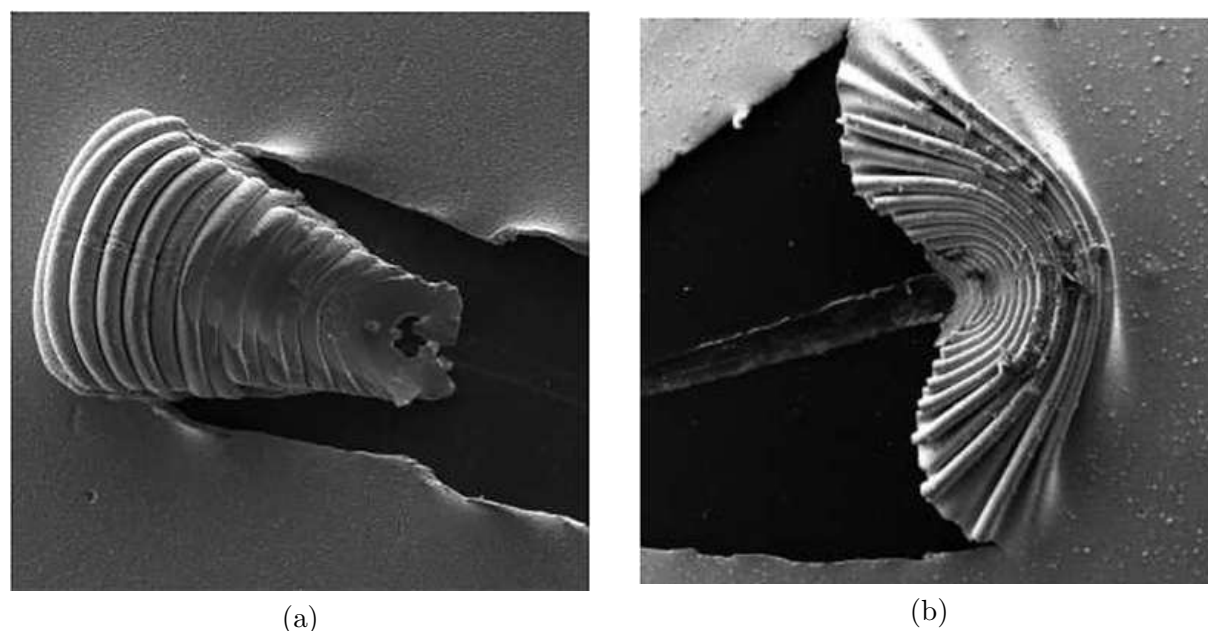


Figure 18. (a) The result of the indenter impact on the lead film deposited on the stainless steel (Aisi 304) surface. The size of the area presented on the figure is 1 mm; (b) the result of the indenter impact on the lead film deposited on the duralumin D16T surface. The size of the area presented on the figure is 3.03 mm.

The average thickness of the direct deposition film in experiment with the carbon sample was $1.3 \mu\text{m}$ and the thickness of the reflected deposition film near collimation inlet (distance from the disk center was about 750 microns) was 35 nm. Figure 15 and formula (2) show that the lead deposition efficiency on the carbon substrates is about 81%. The average substrate temperature during the experiment was about $60 \text{ }^\circ\text{C}$.

Another important question for plasma separation process is the removal of the deposited substance from a surface of the collectors. Results of research of adhesive coverings properties of the lead deposited on the duralumin D16T and stainless steel (Aisi 304) are given below.

Samples were deposited at a temperature within the evaporator of about 900 °C for 2.5 hours. Figure 18 shows traces of the indenters on the lead films with a substrates made from the stainless steel (figure 18a) and duralumin (figure 18b).

In both cases, the connection of covering elements is stronger than the bond of a covering with a surface. The film exfoliation on stainless steel (Aisi 304) begins at a load of 0.45–0.9 N. Exfoliation of a film on duralumin (D16T) begins at a load of 0.35–0.9 N.

From the obtained data it can be concluded that the removal of model substance (lead) from a surface of collectors will not cause difficulties in model experiments.

4. Conclusion

Computational model was built on the basis of the kinetic approach. Ion density distribution, electron density distribution and ionizing efficiency between hot cathode and a point of a local maximum of the potential were found. For the model verification the experiments which confirmed a number of calculated results were carried out. Lead ion current density of about 1 mA/cm² with a potential difference between the cathode and the anode $U_e = 40$ V was obtained in the experiments (the ionization efficiency was about 1%). Analysis of calculated data obtained by the numerical model, allows us to choose the parameters at which the ionizing efficiency in the experiment can be brought to the level of several tens of percent.

Experimental study of deposition processes of substances modeling heavy components of spent nuclear fuel at the various collectors substrate was carried out (duralumin, stainless steel, carbon). The numerical model which allows to select the condensation coefficients, angular function of re-evaporation probability density corresponding to experimental data was created. Lead deposition efficiency on stainless steel and carbon samples was investigated, which was 75% and 81% at medium substrates temperature of 70 °C and 60 °C respectively. Adhesion of the lead coverings on the stainless steel and duralumin substrates was investigated (surface detachment occurs at 0.45–0.9 N and 0.35–0.9 N respectively).

Acknowledgments

The study was supported by the Russian Science Foundation (grant No. 14-29-00231).

References

- [1] Zhil'tsov V A, Kulygin V M, Semashko N N, Skovoroda A A, Smirnov V P, Timofeev A V, Kudryavtsev E G, Rachkov V I and Orlov V V *At. Energy* **101** 755
- [2] Vorona N A, Gavrikov A V, Samokhin A A, Smirnov V P and Khomyakov Y S 2015 *Phys. At. Nucl.* **78** 1
- [3] Smirnov V P, Samokhin A A, Vorona N A and Gavrikov A V 2013 *Plasma Phys. Rep.* **39** 456
- [4] Liziakin G and Usmanov R 2015 *Phys. Procedia* **71** 138
- [5] Amirov R K, Vorona N A, Gavrikov A V, Zhabin S N, Liziakin G D, Polistchook V P, Samoylov I S, Smirnov V P, Usmanov R A and Yartsev I M 2014 *Tr. Moskovsk. Fizikotekh. Inst.* **6** 136
- [6] Antonov N N, Vorona N A, Gavrikov A V, Samokhin A A and Smirnov V P 2016 *Tech. Phys.* **61** 180
- [7] Child C D 1911 *Phys. Rev.* **32** 492
- [8] Langmuir I 1913 *Phys. Rev.* **2** 450
- [9] Nottingham W 1956 *Thermionic Emission* (Massachusetts Institute of Technology) p 178
- [10] Pound G M 1972 *J. Phys. Chem. Ref. Data* **1** 135
- [11] Rapp R A, Hirth J P and Pound G M 1961 *J. Chem. Phys.* **34** 184